Cold Pools as Conveyor Belts of Moisture

Herman F. Fuglestvedt[1] and Haerter O Haerter[2]

[1]University of Oslo
[2]Niels Bohr Institute, University of Copenhagen

November 24, 2022

Abstract

Observations and simulations have found convective cold pools to trigger and organize subsequent updrafts by modifying near-surface temperature and moisture as well as by lifting air parcels at the outflow boundaries. We study the causality between cold pools and subsequent deep convection in an idealized large-eddy simulation by tracking colliding outflow boundaries preceding hundreds of deep convection events. When outflow boundaries collide, their common front position remains immobile, whereas the internal cold pool dynamics continues for hours. We analyze how this dynamics "funnels" moisture from a relatively large volume into a narrow convergence zone. We quantify moisture convergence and separate the contribution from surface fluxes, finding that it plays a secondary role. Our results highlight that dynamical effects are crucial in triggering new convection, even in radiative-convective equilibrium. However, it is the moisture convergence resulting from this dynamics that moistens the atmosphere aloft and ultimately permits deep convection.

Cold Pools as Conveyor Belts of Moisture

Herman F. Fuglestvedt[1,2] and Jan O. Haerter[2]

[1]University of Oslo, 0315 Oslo, Norway
[2]Niels Bohr Institute, University of Copenhagen, Blegdamsvej 17, 2100 Copenhagen, Denmark

Key Points:

- Cold pool collisions cause a sustained reset of moisture circulation;
- Tracking of colliding outflow boundaries highlights the role of pre-moistening in cold pool organization;
- The primary cause of pre-moistening is sustained low-level convergence, surface fluxes play a secondary role.

Corresponding author: Herman F. Fuglestvedt, herman.fuglestvedt@geo.uio.no

Abstract

Observations and simulations have found convective cold pools to trigger and organize subsequent updrafts by modifying near-surface temperature and moisture as well as by lifting air parcels at the outflow boundaries. We study the causality between cold pools and subsequent deep convection in an idealized large-eddy simulation by tracking colliding outflow boundaries preceding hundreds of deep convection events. When outflow boundaries collide, their common front position remains immobile, whereas the internal cold pool dynamics continues for hours. We analyze how this dynamics "funnels" moisture from a relatively large volume into a narrow convergence zone. We quantify moisture convergence and separate the contribution from surface fluxes, finding that it plays a secondary role. Our results highlight that dynamical effects are crucial in triggering new convection, even in radiative-convective equilibrium. However, it is the moisture convergence resulting from this dynamics that moistens the atmosphere aloft and ultimately permits deep convection.

Plain Language Summary

Cold pools are blobs of cold air that can form under thunderstorm clouds due to the evaporation of rain. Because they are denser than the surrounding air, cold pools spread out along the surface. It has long been known that thunderstorm development, while inhibited inside the cold pools, is stimulated near the edges. Here we use idealized numerical simulations of cold pool-producing tropical thunderstorms to study how the cold pools interact to achieve this organization of subsequent clouds. We find that when cold pools collide with one another, they establish a circulation near the surface that lasts for several hours. This circulation transports moist air from a very large area into a small one, where it is deflected upwards and eventually facilitates thunderstorm development. Our results improve our understanding of how cold pools trigger extreme rain events, and have implications for how thunderstorms should be depicted in climate models.

1 Introduction

1.1 Atmospheric cold pools

Cold pools (CPs) form as a fraction of precipitation from a cloud re-evaporates when it falls to the surface. The latent heat absorbed during the phase change cools the air below cloud base, creating a body of relatively dense air that sinks to the ground and spreads laterally. CPs can spread over distances of tens to hundreds of km in the course of one day (Zuidema et al., 2017) and can modify the conditions for subsequent convection by creating and transporting anomalies in temperature, moisture, and wind (e.g. Droegemeier and Wilhelmson (1985); Tompkins (2001); Khairoutdinov and Randall (2006); Knippertz et al. (2009); Böing et al. (2012); Terai and Wood (2013); Feng et al. (2015); Torri and Kuang (2016); de Szoeke et al. (2017)). The edges, where the CPs meet and interact with ambient boundary layer air, are commonly referred to as the *outflow boundaries.*

Deep convective cells have long been known to preferentially form along these outflow boundaries (Purdom & Marcus, 1981; Droegemeier & Wilhelmson, 1985). Two mechanisms explaining this organization have been proposed. The classic and intuitive view is that forced lifting along the advancing outflow boundaries helps parcels of boundary layer air to overcome convective inhibition and reach the level of free convection (LFC) (Droegemeier and Wilhelmson (1985); and more recently Jeevanjee and Romps (2015); Torri et al. (2015)). This was challenged by Tompkins (2001). Instead, in cloud-resolving model simulations of a tropical ocean environment, he observed that convective triggering occurred long *after* the expansive phase of the CPs, which is when the highest wind speeds at the outflow boundaries occur. The key to triggering new deep convection he therefore attributed to a combination of low CIN and high CAPE at the outflow boundary after the CP cold anomaly was recovered by surface fluxes, a mechanism that has found support in later studies (Langhans & Romps, 2015; Torri et al., 2015).

Colliding outflow boundaries create bands of strong updrafts (Wilson & Schreiber, 1986; Lima & Wilson, 2008; Böing et al., 2012), typically explained by either or both of the above mechanisms. Due to low-level convergence, these bands constitute moist patches over which clouds form (Krueger, 1988). Schlemmer and Hohenegger (2014) found that larger moist patches support the formation of more, as well as larger and deeper clouds. This lends support to the "near-environment hypothesis" postulated by Böing et al. (2012), stating that wider cloud bases over colliding outflow boundaries reduce the entrainment of subsaturated air into growing clouds, thus allowing them to retain their buoyancy and develop into cumulonimbi.

Pursuing these findings, Feng et al. (2015) used high-resolution regional model simulations of warm tropical ocean conditions to examine convective organization by CPs. They found colliding CPs to trigger substantially more shallow convection than isolated ones, attributed to enhanced updraft velocities. The increased accumulation of shallow convective clouds, in turn, moistens the environment above the boundary layer, reducing dry-air entrainment and eventually allowing for deep convection to develop. This echoes an earlier study by Waite and Khouider (2010), who found the deepening of cumulus clouds in cloud-resolving numerical experiments to depend heavily on the detrainment of moist air into the environment by congesti preceding the formation of deep convection.

Parametrizations of convection in climate models have struggled to capture the diurnal cycle of convection occurring over tropical land (e.g. Betts and Jakob (2002); Nesbitt and Zipser (2003)). Coupling a convection parametrization scheme with a simple representation of CPs that dynamically allow surface parcels to overcome convective inhibition amended this (Rio et al., 2009; Grandpeix & Lafore, 2010), suggesting that forced lifting by CPs actively organizes convection over land.

Convective conditions over tropical oceans differ from those over land due to the higher heat capacity of the sea surface. The tropical marine atmosphere is therefore subject to near-constant surface heating, and is often approximated as residing in a state of radiative-convective equilibrium (RCE) which cannot produce a diurnal cycle of convection. Thus, there is reason to believe that the ways in which CPs organize and trigger convection are also different, as the results of, e.g., Tompkins (2001) show.

Which mechanisms are behind triggering of deep convection under which conditions is still contested in the literature. In any case, CPs doubtlessly are a key ingredient in the organization of convection and the transition from shallow to deep convection. In this study, we characterize the causality between CPs and subsequent convection using large-eddy simulations (LES). To do so, we exploit an idealized setup that permits a simple tracking of the convergence zones established by colliding outflow boundaries. Furthermore, we ask what the contribution of surface fluxes is to the moisture convergence.

2 Methodology

2.1 Large-eddy simulations

Three idealized large-eddy simulations (LES) are run using the University of California, Los Angeles (UCLA) LES code (Stevens et al., 2005) (*see* Supplementary Information). We perform three simulations with a varying surface boundary condition: a control simulation (termed CTR) with a surface at 300 K and 100 % relative humidity, compared to a simulation with a 2 K colder surface (termed -2K) and a simulation with a surface relative humidity of 70 % (termed RH70). CTR and -2K correspond to tropical ocean conditions (Bowen ratios of ~ 0.1), while RH70 is representative for tropical rainforest conditions (Bowen ratio of ~ 0.25).

To achieve radiative convective equilibrium (RCE), surface temperature and humidity, as well as insolation are held constant throughout each simulation. We here study the properties within RCE, attained after 300 model hours for CTR and -2K, and 150 model hours for RH70. These thresholds were chosen as the times when the spatial averages of near-surface temperature and humidity were converged to the equilibrium values. See Supplementary Information for details.

2.2 Idealized setup

Focusing on diurnal cycle dynamics, Haerter et al. (2019) highlights the complexity of CP interactions within the three-dimensional atmosphere. In that case, several geometrical configurations of CP collisions can occur, and those involving two and three CPs were found to be conceptually different. In order to remove the complexities introduced by the different geometries of collision, and focus entirely on the processes that are active in the lead-up to the formation of new convective events after a collision, we use an idealized setup: the LES is run at a $200\,\text{km}\times 5\,\text{km}$ horizontal grid resolution and the output averaged over the narrow dimension before analysis. This pseudo-2D setup hence resembles air embedded in a channel, where spreading CPs are forced to travel along the direction of the channel. This is enforced by the laterally periodic boundary conditions, as a CP's outflow along the narrow dimension will soon collide with the same CP's opposite edge, effectively limiting the direction of motion to be along the long dimension. For a further discussion, *see* Supplementary Information.

2.3 Simple tracking of outflow boundaries

An advantage of the above described setup is that the causality between colliding outflow boundaries, loci of convergence, and subsequent deep convection becomes apparent. In order to study the evolution of the atmosphere at the loci of convergence in the hours leading up to a new convective event, a tracking algorithm is used: our algorithm identifies these loci preceding every convective precipitation event. The events are identified by first locating precipitation intensity peaks in the spatial dimension that exceed $1\,\text{mm}\,\text{h}^{-1}$. An upper threshold of 160 min on the duration of precipitation events is then assumed, as well as the fluctuation in the location of the precipitation intensity peak to not exceed 4 km from the location of the earliest peak. This allows for the definition of precipitation onset as the time of the earliest of these peaks, from which the tracking algorithm identifies the loci of convergence backwards in time. These are defined as the maxima of near-surface vertical velocity, searching in the vicinity of the last point on the track. This vicinity is chosen as the area within 4 km from the last point, in effect assuming that the convergence locus is not advected further in a single timestep, corresponding to a speed of $\sim 6.7\,\text{m}\,\text{s}^{-1}$. The search is terminated when the track leads to the vicinity of a preceding deep convection event. If this condition is not met, the search is terminated when the tracking exceeds 80 timesteps, corresponding to 13.3 model hours.

3 Results

3.1 Identifying precipitation events and convergence loci

To understand the CP dynamics in the present channel domain, it is instructive to focus on a specific vertical model level and consider any output field within the horizontal coordinate as well as time (Figure 1a-c). CPs travel along the surface and their outflow boundaries are visible as sharp spikes in vertical velocity. These spikes correspond to sharp gradients in horizontal velocity, that is, loci of strong horizontal convergence. The convergence patterns are mirrored by the patterns found in near-surface moisture,

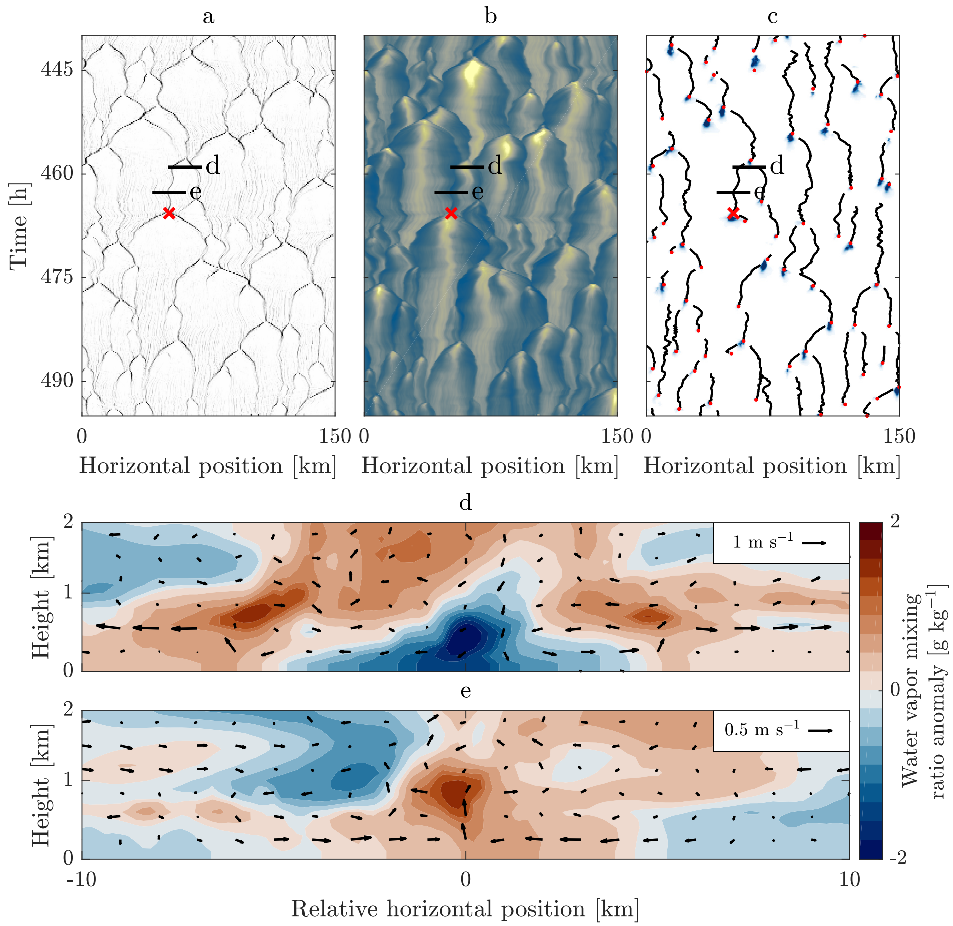

Figure 1. Cold pool dynamics in the LES (CTR experiment). (a) Near-surface (100 m) vertical velocity. Dark shades indicate positive values. (b) Near-surface (50 m) water vapor mixing ratio. CP interiors are dry (yellow), and outflow boundaries moist (blue) (same color axis as in Figure 3a). (c) Simple tracking of precipitation events (red dots) and preceding convergence loci (black lines) plotted over precipitation intensity (blue shading). Red x marks the time and position of the precipitation event analyzed in Figure 3. Black horizontal lines mark times and positions of vertical cross sections plotted in panels d, e. (d, e) Vertical cross sections of water vapor mixing ratio anomaly (contours) and wind (vectors). For clarity, the wind is subtracted by the horizontal mean flow in the plotted sub-domain, and velocities are averages of bins of 5 and 3 grid points (corresponding to 1000 m and 300 m) in the horizontal and vertical dimension, respectively.

with water vapor mixing ratio increasing near the colliding outflow boundaries, or "collision fronts" (Figure 1b). Inspecting this convergence pattern further, it is apparent that the collision fronts are also the locations where new deep convection events occur (Figure 1c). Although both outflow boundaries usually contribute large vertical velocities as the boundaries collide, inspection shows that new events typically occur at the collision front several hours after the collision occurred. This suggests that the immediate mechanical lifting of boundary layer parcels to the LCL plays little role in the triggering of new events in RCE. Instead, we here argue that the circulation surrounding the collision front continues, long after the time when the outflow boundaries initially collide, allowing moist near-surface air to be continuously lifted within the convergence zone.

To qualitatively appreciate this, the moisture circulation during two phases of the CP's lifetime is plotted in Figure 1d,e. Strong vertical velocities accompany the horizontal velocities at the outflow boundary during the early expansive phase (Figure 1d). However, even more than 4 h after the CP outflow boundary has been stalled by that of the neighbouring CP, moisture continues to circulate, converging at the collision front, where it is advected to higher levels and constitutes a moisture anomaly (Figure 1e). This convergence continues for a few hours more at more or less the same position before a new deep convection event occurs.

To show that such sustained CP-induced convergence zones are the most important mechanism behind organizing deep convection in the numerical experiments, we use the tracking algorithm described in section 2.3 to aggregate the loci of these convergence zones in the buildup to deep convection events.

3.2 Aggregate statistics during event buildup

In our idealized setup, the tracking of convergence loci preceding deep convection permits sampling of the local atmospheric properties. Note that in three-dimensional analogues such tracking would be far more cumbersome: outflow boundaries would be line structures and the cross-section upon collisions of any two or more outflow boundaries would have far more complex geometries than in the case we study here — introducing additional degrees of freedom into the analysis.

Using the backtracking for all detected deep convective events, we recover the history of instability and moisture during the time leading up to the event (Figure 2). The track duration, that is, the time between precipitation onset and the time when the backtracking is terminated, is different from event to event. For the aggregate buildup, a duration starting at -8 h is chosen, as the frequencies of track durations longer than this drops below 5 % for all three numerical experiments. (Figure S3). At the other end, the aggregate buildup is truncated at 20 min before precipitation onset. The quantities plotted in Figure 2 all exhibit a sudden change after this, which we attribute to the effects of downdrafts forming in the minutes before precipitation onset and occurrence of imprecisely timed precipitation onsets. This time window of -8 h to -20 min is used for the results reported here. The untruncated time evolution of the quantities, as directly obtained by the tracking procedure described in section 2.3, are plotted in Figure S4.

Classical measures of convective instability are CAPE and CIN (*see* Supplementary Information). Indeed, CAPE (Figure 2c) is appreciable and increases systematically before event onset. CIN requires a more careful inspection, as near-surface parcels are relatively moist and show very small values of CIN ≈ 0 throughout the lead-up to the new event. Accompanied by the appreciable CAPE, this lack of inhibition implies deep convection onset according to parcel theory. To evaluate the maximum inhibition in the boundary layer, we define the boundary layer as bounded above by the mean LFC in each experiment ($\overline{\mathrm{LFC}}$) and pick the most stable parcel, for which convective inhibition henceforth is termed *max-CIN*. Although slightly larger, max-CIN is also negligible (Figure 2d). The gradual reduction in max-CIN indicates that moisture is transported up to the

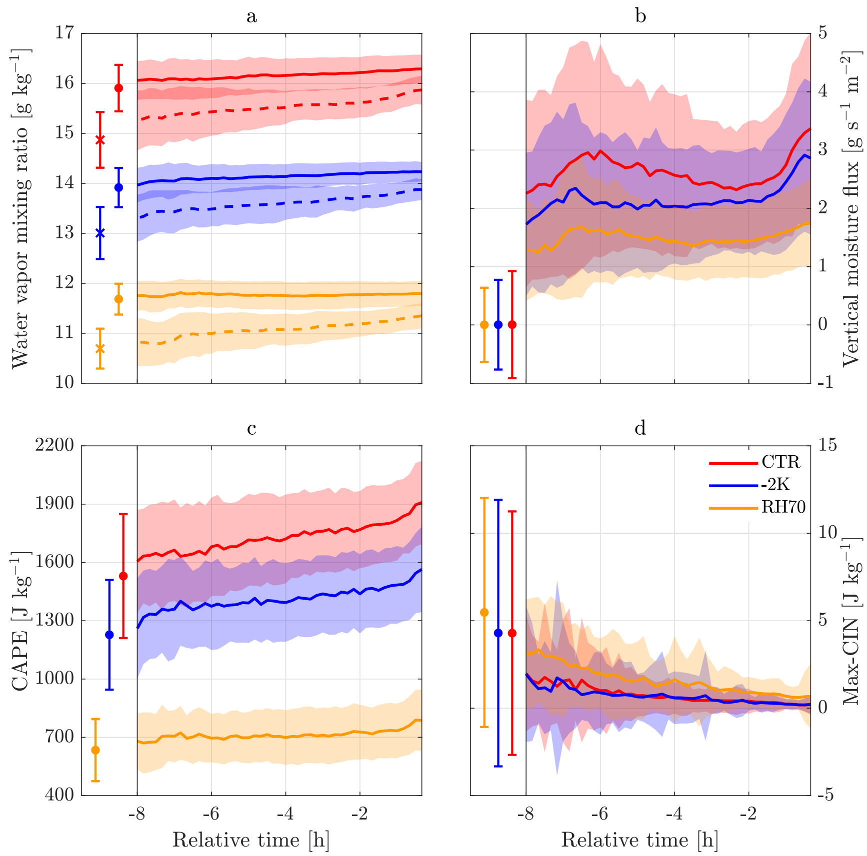

Figure 2. Time evolution of aggregate atmospheric properties at the tracked convergence loci. The time axis is relative to the precipitation onset at 0 h. (a) Water vapor mixing ratio near surface (50 m) (solid) and at mean level of free convection ($\overline{\mathrm{LFC}}$) (dashed). (b) Near-surface (100 m) vertical moisture flux ($qw\rho$). (c) Convective available potential energy (CAPE). (d) Convective inhibition (CIN) for the most inhibited boundary layer reference parcel ($z \leq \overline{\mathrm{LFC}}$). Solid/dashed lines are mean values and shading indicates one standard deviation of the aggregate. Left-side markers and errorbars show the system mean values and one standard deviation for the plotted quantities (dot and x correspond to solid and dashed, respectively).

Table 1. Aggregate statistics during event buildup[a]

	CTR	-2K	RH70	Units
Δq(50 m)	0.2 ± 0.5	0.3 ± 0.4	0.0 ± 0.4	$\mathrm{g\,kg^{-1}}$
Δq($\overline{\mathrm{LFC}}$)	0.6 ± 0.7	0.6 ± 0.5	0.5 ± 0.5	$\mathrm{g\,kg^{-1}}$
IVMF(100 m)	74 ± 6	61 ± 5	42 ± 3	$\mathrm{kg\,m^{-2}}$
IVMF($\overline{\mathrm{LFC}}$)	60 ± 10	49 ± 9	23 ± 5	$\mathrm{kg\,m^{-2}}$
Model level of $\overline{\mathrm{LFC}}$	600	600	1102.5	m

[a]Mean $\pm$ one standard deviation.

higher levels of the boundary layer where the most inhibited parcels typically reside. This moisture transport takes place over the course of hours and thereby can achieve the reduction in inhibition there.

Figure 2a shows that near-surface moisture increases modestly along the collision front until new deep convection sets in, whereas the increase at the $\overline{\mathrm{LFC}}$ is several times larger (dashed curves). The moisture increase, Δq, is reported in Table 1. The order of magnitude of Δq($\overline{\mathrm{LFC}}$) implies an increase of virtual potential temperature of $\sim 0.1\,\mathrm{K}$, or an increase in buoyancy of $0.003\,\mathrm{m\,s^{-2}}$ for a constant environmental virtual temperature. As can be seen in Figure 2b, the near-surface vertical moisture flux ($= qw\rho$, where q is water vapor mixing ratio, w is vertical velocity, and ρ is the density of air) remains positive for the duration of the buildup, advecting large quantities of water vapor over the 8 hours. Integrating this quantity over the buildup yields the time-integrated vertical moisture flux (IVMF), reported in Table 1. IVMF($\overline{\mathrm{LFC}}$) is $\sim$80 % of IVMF(100 m) in CTR and -2K, and $\sim$55 % in RH70, indicating that the majority of the converged moisture that is deflected near the surface makes it out of the boundary layer. The above findings suggest that, rather than instability in terms of CAPE/CIN, it is the moistening of the atmospheric column that ultimately permits deep convection.

3.3 The origin and fate of converged moisture

To substantiate this claim, we now turn to study the source of moisture that is deflected into the vertical in the convergence zone, and the eventual moistening of the atmosphere. It is straightforward to compute the accumulated horizontal moisture convergence, C, at vertical level z between time t_i and t_f, by considering the time-integrated difference

$$C \approx \frac{\rho(z)\delta z(z)\Delta t}{x_r - x_l} \sum_{t=t_i}^{t_f} \Big(q(z, x_l, t) v_h(z, x_l, t) - q(z, x_r, t) v_h(z, x_r, t) \Big), \tag{1}$$

where Δt is the output timestep, $q(z, x, t)$ is the water vapor mixing ratio at horizontal position x and time t, $v_h(z, x, t)$ is the corresponding horizontal velocity, x_l and x_r are the horizontal positions of the left and right boundaries defining the convergence zone, taken to be 2 km to either side, $\delta z(z)$ is the vertical grid spacing, and $\rho(z)$ is the air density.

To quantify how much of the moisture increase is due to surface moisture fluxes, we repeat the calculation in equation (1), but replace $q(x_l, t)$ and $q(x_r, t)$ by $q(x'_l, t'_l)$ and $q(x'_r, t'_r)$, where the transformed values x' result from x by iterative backtracking:

$$x(t - \delta t) \to x(t) - \delta t\; v_h(x, t)\ , \tag{2}$$

where $\delta t > 0$ is chosen sufficiently small. This backwards advection is repeated $n \equiv (t{-}t')/\delta t$ times, the required number of iterations to reach (x', t'), the location and time of the preceding downdraft on each side of the convergence zone. This procedure essentially replaces the value of q at the convergence zone boundary by a modified value, which would be present if moisture was only advected horizontally and no surface fluxes were present during the parcel's journey towards the convergence zone. In fact, moisture is also advected vertically, but vertical velocities contribute little ($\sim 2\,\%$) of the wind speed in the regions that are neither convergence zones nor downdrafts (Figure S2). Our analysis hence leaves us with an approximation to the surface flux contribution to the moisture convergence in the time between formation of CPs and the event they trigger.

Figure 3a shows the analysis conducted on a case in CTR (same as Figure 1d,e). The parcels at the boundaries of the convergence zone follows paths originating in the dry centers of the preceding left and right CPs. Like conveyor belts of moisture, the near-surface circulation set up by the CPs (Figure 3b) transports boundary layer air into the convergence zone, where the convergence deflects it into the vertical. Note that the horizontal near-surface velocities are directed towards the convergence zone for several kilometers to each side, maintaining a large "catchment area" for the convergence zone. This leads to a moistening throughout the atmospheric column over the convergence zone during the buildup to the new deep convective event (Figure 3c). Using equation (1) to approximate the near-surface accumulated horizontal moisture convergence starting at the earliest time that the convergence locus is identified, shows that the moisture converges below the $\overline{\text{LFC}}$ at 600 m (Figure 3d). Moisture convergence above this level is negative despite the increase in total water mixing ratio, implying that moisture is vertically advected out of the boundary layer before being detrained into the environment. The total near-surface moisture convergence over the duration of the lead-up amounts to $13.9\,\text{kg}\,\text{m}^{-2}$. Using instead the values $q(x', t')$ in the calculation of near-surface moisture convergence, the amount is $13.0\,\text{kg}\,\text{m}^{-2}$. In other words, surface moisture fluxes contribute only $\sim 6\,\%$ of the total moisture entering the convergence zone in the time between CP formation and subsequent event. The partitioning into advective and moisture source contributions shows that the circulation set up by the colliding outflow boundaries, that persists for hours, acts as moisture conveyor belts on each side of the convergence zone. These extend ~ 10 km to the sides, corresponding to the radii of the CPs. Over the duration of the buildup, the velocities increase, especially in the last hours (Figure 3b). This suggests that the circulation initiated by the CPs sustains and amplifies itself through convection in the convergence zone.

Note that this analysis considers the convergence of moisture during the time between the onset of the new event and the CP formation under the right-side preceding one, illustrated by the red line in Figure 3a. As can be seen, a moist patch is already present at the beginning of this time period, which can explain the discrepancy between the $13.9\,\text{kg}\,\text{m}^{-2}$ that enter the convergence zone through advection and the almost four times higher average near-surface vertical moisture flux observed at the aggregate convergence loci (Table 1). This highlights how each event can not be considered an independent case, but that the continuous "funneling" of moisture into concentrated patches by generations of CP-forming deep convection events predetermines the locations of subsequent ones.

4 Discussion

Our results support the view that preconditioning must occur before deep convective clouds can form – instability, the presence of high CAPE and low CIN, is insufficient. The continuous moistening of the atmospheric column over convergence zones established by CPs provide this preconditioning. Our results resonate in part with mechanisms hypothesized in previous studies. The near environment hypothesis (Böing et al., 2012; Schlemmer & Hohenegger, 2014) is by Feng et al. (2015) described as preconditioning acting through an increased number of shallow clouds that shield deepening clouds from the subsaturated environment. These shallow clouds are a result of the dynamical forcing along collisions fronts, they argue, based on the occurrence of higher verti-

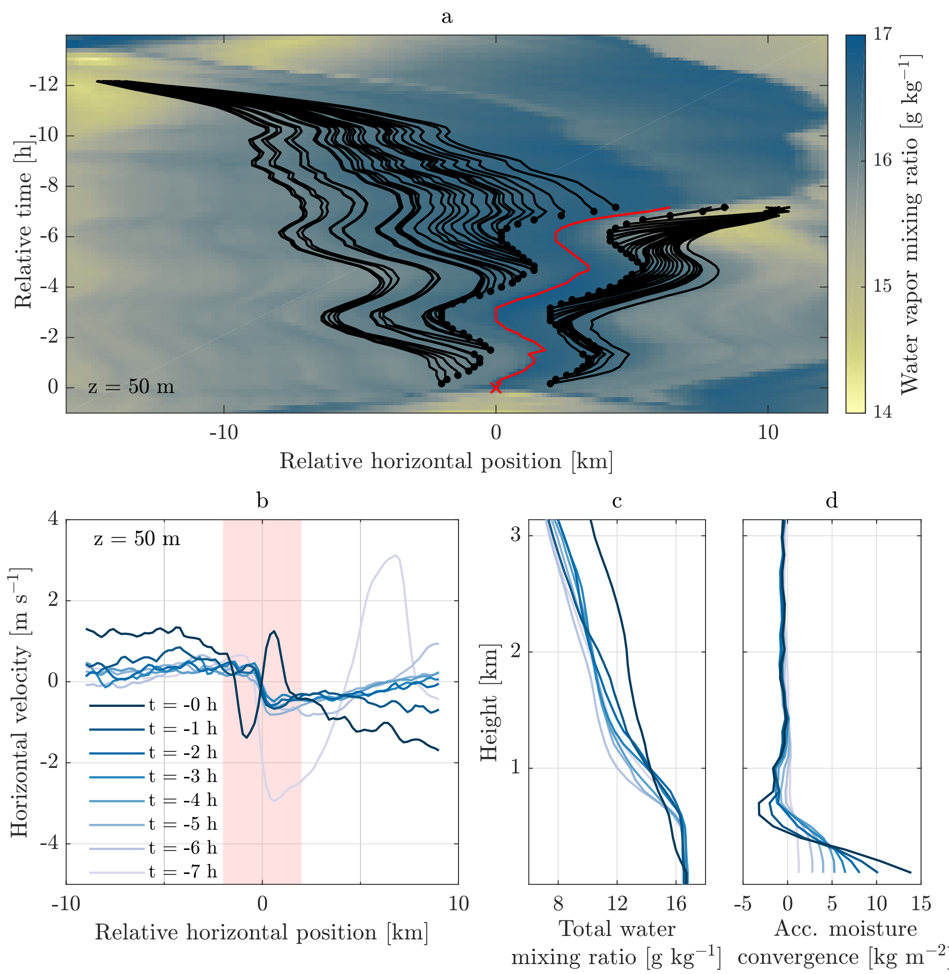

Figure 3. Identifying the contribution from surface moisture fluxes to a deep convection event in CTR. (a) Near-surface water vapor mixing ratio. Positions of parcels (black dots) in the vicinity of convergence locus (red line) preceding a deep convection event (red x) advected backwards in time (black lines) to origins in previous downdrafts. Position is relative to the precipitation event. (b) Time evolution of the horizontal profile of near-surface (50 m) horizontal wind. Position is relative to the convergence locus. Red patch indicates the area taken as the convergence zone bounded by the black dots in a. (c) Time evolution of the vertical profile of total water mixing ratio at the convergence locus. (d) Time evolution of the vertical profile of accumulated horizontal moisture convergence, where the convergence is approximated according to equation 1.

cal velocities over colliding outflow boundaries. However, our results draw focus instead to the near-surface circulation set up by the CPs. Rather than the preconditioning aloft being controlled by the strength of forced uplift in the expanding phase of the CPs, we find that the slow and consistent moisture convergence near the surface establishes long-lasting convergence zones, constituting moist patches (Schlemmer & Hohenegger, 2014), that in turn moisten the atmosphere above. This resonates better with the second idea put forward by Böing et al. (2012), the "time scale hypothesis", which suggests that the role of the subcloud layer is to establish updrafts lasting long enough to permit cloud deepening. As they point out, these loci will be subject to a positive feedback, as once deeper clouds form, they will amplify the underneath convergence and further the advantage over other locations for deep convection. How the maintenance of the convergence zone is divided between the original CP circulations and this positive feedback, we have not attempted to quantify here, but we interpret the results to clearly show that colliding outflow boundaries are necessary to initialize the circulation.

The type of "pseudo-2D" geometric setup exploited in this study helps to clarify the causality between CPs, moisture convergence, and subsequent deep convection, and permits a simple way of tracking it. We assume that our conclusions about the mechanisms at work in this setup also apply to the 3D analogy, where the horizontal dimensions would be of equal scale. The basic principle that each deep convection event on average spawns one new one necessarily holds true in the 3D case as well. This is an inevitable consequence of the fact that we are considering an RCE state, where the number of simultaneous events is constant. However, there are a few subtle differences to the 3D case. As earlier discussed (*see* Methodology) a 3D domain permits both 2CP and 3CP collisions. In the current setup, where CPs are confined to move along only one horizontal dimension, all collisions are effectively 3CP collisions since the air trapped between two CPs is forced to escape vertically. Thus, the dynamical effect of CP collisions could be overestimated (Figure S5). However, our findings suggest that the immediate forced lifting in the moment when CPs collide is incapable of triggering deep convection and that the slower process of funneling moisture into convergence zones dominates in RCE. The possible overestimation of the dynamical effect is therefore inconsequential.

5 Summary and conclusions

This study aimed to clarify the mechanisms with which CPs organize and initiate new deep convection events in RCE. Large-eddy simulations run in an idealized 2D-like setup elucidate the causal relationships between CPs, moisture convergence, and deep convection triggering: Where outflow boundaries collide, the interaction of the circulation within each CP establishes narrow convergence zones in the boundary layer that persist for hours, sustained by "conveyor belts" of moisture on either side. As moisture from a several kilometers wide "catchment area" is advected into the convergence zone and deflected vertically, the atmosphere above moistens gradually. Tracking the loci of convergence shows that the aggregate convergence locus experiences negligible CIN and large CAPE from the start, several hours before deep convection occurs. The near-surface vertical moisture flux remains positive, ~ 1–$3\ \mathrm{g\,s^{-1}\,m^{-2}}$ depending on the surface boundary condition, over the whole duration, steadily increasing the water vapor mixing ratio above the boundary layer.

This mechanism is illustrated by a closer analysis of a single deep convection event and its buildup in the LES. We find that the CPs on either side preceding the event establish a circulation where near-surface moisture is funneled into a narrow convergence zone from an area $\sim$10 km to either side. The contribution of surface moisture fluxes during this time to the total moisture that enters the convergence zone is relatively little (6 %). In the convergence zone, the converging moisture inevitably ascends and leads to a moistening of the atmospheric column despite horizontal moisture divergence above the boundary layer. This corroborates the evidence found in the aggregate of tracked convergence loci for a gradual preconditioning of the atmosphere over convergence zones established by colliding outflow boundaries.

Acknowledgments

HFF and JOH gratefully acknowledge funding by a grant from the VILLUM Foundation (grant number: 13168) and the European Research Council (ERC) under the European Union's Horizon 2020 research and innovation program (grant number: 771859). We acknowledge the Danish Climate Computing Center (DC3). Data used in this study are archived and available under the doi https://doi.org/10.11582/2020.00008.

References

Betts, A. K., & Jakob, C. (2002). Evaluation of the diurnal cycle of precipitation, surface thermodynamics, and surface fluxes in the ecmwf model using lba data. *Journal of Geophysical Research: Atmospheres*, *107*(D20), LBA–12.

Böing, S. J., Jonker, H. J., Siebesma, A. P., & Grabowski, W. W. (2012). Influence of the subcloud layer on the development of a deep convective ensemble. *Journal of the Atmospheric Sciences*, *69*(9), 2682–2698.

de Szoeke, S. P., Skyllingstad, E. D., Zuidema, P., & Chandra, A. S. (2017). Cold pools and their influence on the tropical marine boundary layer. *Journal of the Atmospheric Sciences*, *74*(4), 1149–1168.

Droegemeier, K. K., & Wilhelmson, R. B. (1985). Three-dimensional numerical modeling of convection produced by interacting thunderstorm outflows. part i: Control simulation and low-level moisture variations. *Journal of the atmospheric sciences*, *42*(22), 2381–2403.

Feng, Z., Hagos, S., Rowe, A. K., Burleyson, C. D., Martini, M. N., & de Szoeke, S. P. (2015). Mechanisms of convective cloud organization by cold pools over tropical warm ocean during the amie/dynamo field campaign. *Journal of Advances in Modeling Earth Systems*, *7*(2), 357–381.

Grandpeix, J.-Y., & Lafore, J.-P. (2010). A density current parameterization coupled with emanuels convection scheme. part i: The models. *Journal of the Atmospheric Sciences*, *67*(4), 881–897.

Haerter, J. O., Böing, S. J., Henneberg, O., & Nissen, S. B. (2019). Circling in on convective organization. *Geophysical Research Letters*.

Haerter, J. O., & Schlemmer, L. (2018). Intensified cold pool dynamics under stronger surface heating. *Geophysical Research Letters*, *45*(12), 6299–6310.

Jeevanjee, N., & Romps, D. M. (2015). Effective buoyancy, inertial pressure, and the mechanical generation of boundary layer mass flux by cold pools. *Journal of the Atmospheric Sciences*, *72*(8), 3199–3213.

Khairoutdinov, M., & Randall, D. (2006). High-resolution simulation of shallow-to-deep convection transition over land. *Journal of the atmospheric sciences*, *63*(12), 3421–3436.

Knippertz, P., Trentmann, J., & Seifert, A. (2009). High-resolution simulations of convective cold pools over the northwestern sahara. *Journal of Geophysical Research: Atmospheres*, *114*(D8).

Krueger, S. K. (1988). Numerical simulation of tropical cumulus clouds and their interaction with the subcloud layer. *Journal of the atmospheric sciences*, *45*(16), 2221–2250.

Langhans, W., & Romps, D. M. (2015). The origin of water vapor rings in tropical oceanic cold pools. *Geophysical Research Letters*, *42*(18), 7825–7834.

Lima, M. A., & Wilson, J. W. (2008). Convective storm initiation in a moist tropical environment. *Monthly Weather Review*, *136*(6), 1847–1864.

Nesbitt, S. W., & Zipser, E. J. (2003). The diurnal cycle of rainfall and convective intensity according to three years of trmm measurements. *Journal of Climate*, *16*(10), 1456–1475.

Pincus, R., & Stevens, B. (2009). Monte carlo spectral integration: A consistent approximation for radiative transfer in large eddy simulations. *Journal of Advances in Modeling Earth Systems*, *1*(2).

Purdom, J., & Marcus, K. (1981). Thunderstorm trigger mechanisms over the southeast united-states. In *Bulletin of the american meteorological society* (Vol. 62, pp. 1423–1423).

Rio, C., Hourdin, F., Grandpeix, J.-Y., & Lafore, J.-P. (2009). Shifting the diurnal cycle of parameterized deep convection over land. *Geophysical Research Letters*, *36*(7).

Schlemmer, L., & Hohenegger, C. (2014). The formation of wider and deeper clouds as a result of cold-pool dynamics. *Journal of the Atmospheric Sciences*, *71*(8), 2842–2858.

Seifert, A., & Beheng, K. (2006). A two-moment cloud microphysics parameterization for mixed-phase clouds. part 1: Model description. *Meteorology and atmospheric physics*, *92*(1-2), 45–66.

Smagorinsky, J. (1963). General circulation experiments with the primitive equations: I. the basic experiment. *Monthly weather review*, *91*(3), 99–164.

Stevens, B. (2010). *Introduction to ucla-les.*

Stevens, B., Moeng, C.-H., Ackerman, A. S., Bretherton, C. S., Chlond, A., de Roode, S., ... others (2005). Evaluation of large-eddy simulations via observations of nocturnal marine stratocumulus. *Monthly weather review*, *133*(6), 1443–1462.

Terai, C., & Wood, R. (2013). Aircraft observations of cold pools under marine stratocumulus. *Atmospheric Chemistry and Physics*, *13*(19), 9899–9914.

Tompkins, A. M. (2001). Organization of tropical convection in low vertical wind shears: The role of cold pools. *Journal of the atmospheric sciences*, *58*(13), 1650–1672.

Torri, G., & Kuang, Z. (2016). Rain evaporation and moist patches in tropical boundary layers. *Geophysical Research Letters*, *43*(18), 9895–9902.

Torri, G., Kuang, Z., & Tian, Y. (2015). Mechanisms for convection triggering by cold pools. *Geophysical Research Letters*, *42*(6), 1943–1950.

Waite, M. L., & Khouider, B. (2010). The deepening of tropical convection by congestus preconditioning. *Journal of the Atmospheric Sciences*, *67*(8), 2601–2615.

Wilson, J. W., & Schreiber, W. E. (1986). Initiation of convective storms at radar-observed boundary-layer convergence lines. *Monthly Weather Review*, *114*(12), 2516–2536.

Zuidema, P., Torri, G., Muller, C., & Chandra, A. (2017). A survey of precipitation-induced atmospheric cold pools over oceans and their interactions with the larger-scale environment. *Surveys in Geophysics*, *38*(6), 1283–1305.

Supplementary Information

S5.1 UCLA LES

The UCLA LES incorporates an interactive radiative transfer computation (Pincus & Stevens, 2009), and a two-moment cloud microphysics parametrization scheme (Seifert & Beheng, 2006) to allow for rain re-evaporation. Surface energy fluxes are described interactively through Monin-Obukhov similarity theory. The latent and sensible heat fluxes entering the atmosphere through the surface thereby vary spatially, increasing at locations of larger surface wind speed. The model uses the Arakawa C-grid and is run at a 200 m horizontal resolution with periodic boundary conditions in the horizontal dimensions. The vertical dimension consists of 75 levels, with a resolution of 100 m below 1 km, gradually increasing to 400 m towards the model top located at 16.5 km. The lower boundary condition, given by surface temperature and humidity is homogeneous across the flat domain. The solar zenith angle is taken as a constant equal to the daily average for tropical insolation (50.5°). Subgrid-scale turbulent fluxes are parametrized according to the Smagorinsky model (Smagorinsky, 1963). Further technical details can be found in the UCLA-LES reference manual (Stevens, 2010).

The equilibrium values of near-surface temperature and humidity were estimated by fitting the exponential $Q(t) = Q_{eq} - Q_0 \cdot \exp(-t/t_0)$ to the convergence towards the equilibrium state (Figure S1). Here Q_{eq} is the equilibrium value, Q_0 the difference $Q_{eq} - Q(t = t_i)$ where t_i is the initial time of the fit, chosen to reduce the impact of spin-up oscillations, and t_0 the inverse rate of approach to the equilibrium state. The initial conditions were chosen as in Haerter and Schlemmer (2018), but are irrelevant for the RCE state. In this state, the imbalance in energy fluxes entering and leaving the system is small, and is not considered to influence the conclusions drawn here.

S5.2 Diagnosing atmospheric stability

Stability within each grid cell of the LES is here considered by computing convective available potential energy (CAPE) and convective inhibition (CIN), defined as

$$\mathrm{CAPE} = g \sum_{z=\mathrm{LFC}}^{\mathrm{LNB}} \frac{T_{\mathrm{vp}} - T_{\mathrm{ve}}}{T_{\mathrm{ve}}} \delta z \tag{S1}$$

$$\mathrm{CIN} = -g \sum_{z=z_0}^{\mathrm{LFC}} \frac{T_{\mathrm{vp}} - T_{\mathrm{ve}}}{T_{\mathrm{ve}}} \delta z, \tag{S2}$$

where g is the acceleration due to gravity, δz the grid spacing in the vertical z-coordinate, and T_{vp} and T_{ve} the virtual temperature of the reference parcel and the environment, respectively. The limits of integration – the level of free convection (LFC) and level of neutral buoyancy (LNB) – are found by first identifying the lifting condensation level (LCL), taken as the level where the vapor pressure of the reference parcel at the level z_0, retaining its water vapor mixing ratio throughout ascent, equals the saturation vapor pressure along the dry adiabat corresponding to the temperature at z_0. Above the LCL, the parcel temperature T_{p} and water vapor mixing ratio q_{p} is found iteratively by computing the moist adiabatic lapse rate Γ_m at every level according to

$$\Gamma_m = g \frac{1 + L_{\mathrm{v}} q_{\mathrm{p}} / R T_{\mathrm{p}}}{c_p + L_{\mathrm{v}}^2 q_{\mathrm{p}} \epsilon / R T_{\mathrm{p}}^2}, \tag{S3}$$

where L_v is the latent heat of vaporization, c_p the specific heat at constant pressure of dry air, R the gas constant for dry air, and ϵ the ratio of the gas constants for dry air and for water vapor. The parcel is assumed to be saturated at every level above the LCL. The resulting parcel virtual temperature profile, by comparison to the ambient virtual temperature profile, yields the grid cell atmospheric stability in terms of CAPE and CIN.

S6 Idealized setup

Haerter et al. (2019) highlights the complexity of interactions between two or three CPs (2CP and 3CP collisions) within the three-dimensional atmosphere. In 2CP collisions, boundary layer air displaced by the outflow boundaries as they collide, can escape either vertically or laterally, whereas in 3CP collisions the resulting outflow is confined to the vertical dimension. Furthermore, in 3CP collisions, the geometry must be such that the air is captured between the colliding outflow boundaries for this to be the case (*see* Figure 3a in Haerter et al. (2019)). Since motion in the channel-like pseudo-2D setup is confined in the narrow dimension, all collisions effectively act like the 3CP collisions in the three dimensional problem, where air must be forced upward. Vertical velocities, and the dynamical effect of CP collisions, can therefore be expected to be overestimated, as lateral escape is never possible. Furthermore, the rapid and inevitable collision of every CP with its own opposite edge in the narrow dimension may decrease the speed of the outflow boundary in the long dimension, due to turbulent kinetic energy generation. Comparing velocities to those in a similar 3D setup shows that horizontal velocities are slightly lower ($\sim$11 % lower on average, Figure S5) and vertical velocities slightly higher in the pseudo-2D setup (Figure S5), in accordance with the above considerations.

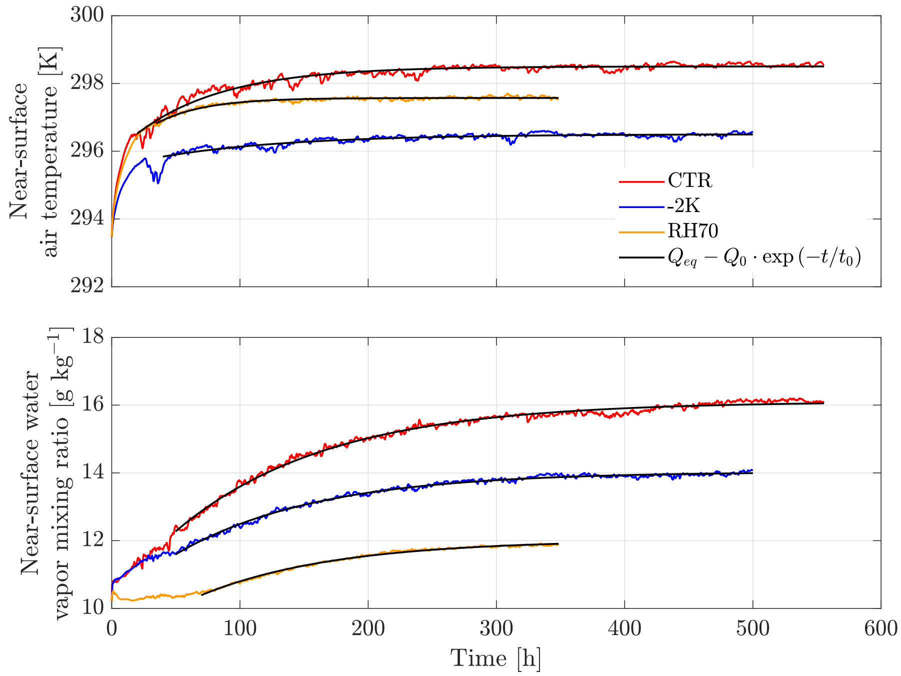

Figure S1. Mean near-surface (50 m) air temperature and water vapor mixing ratio in the three numerical experiments, overlaid by fitted exponential functions.

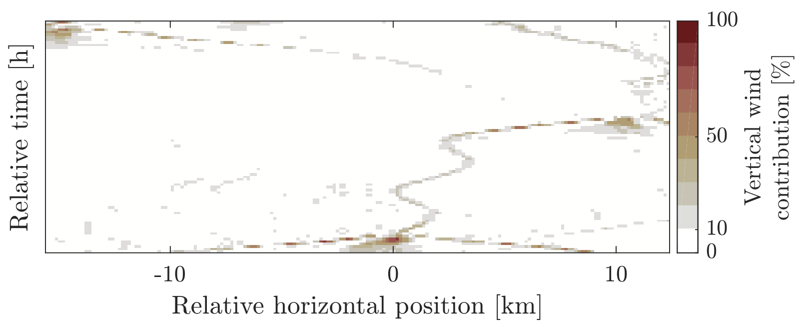

Figure S2. The contribution of vertical wind to the total wind in the area plotted in Figure 3a. The contribution is expressed by the ratio $|w|/\langle\sqrt{v^2+w^2}\rangle \times 100$, of the vertical wind speed $|w|$ to the total velocity averaged over the plotted sub-domain, $\langle\sqrt{v^2+w^2}\rangle$, where v is the horizontal velocity.

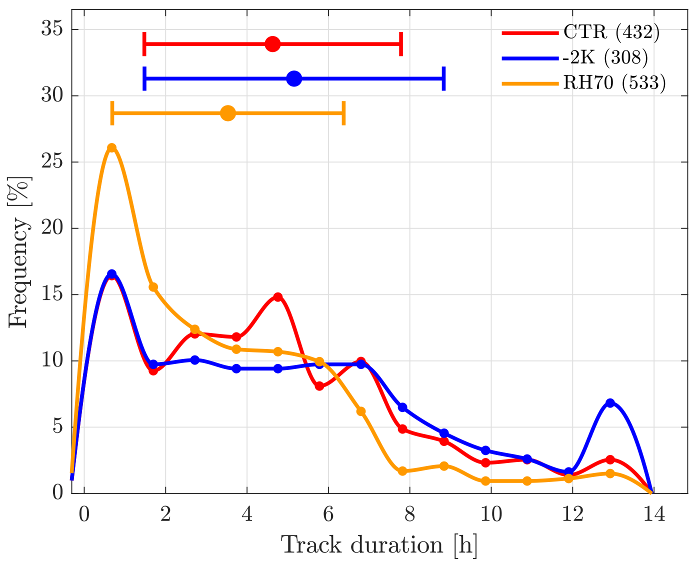

Figure S3. Duration of tracked convergence loci in the three numerical experiments (n given in legend).

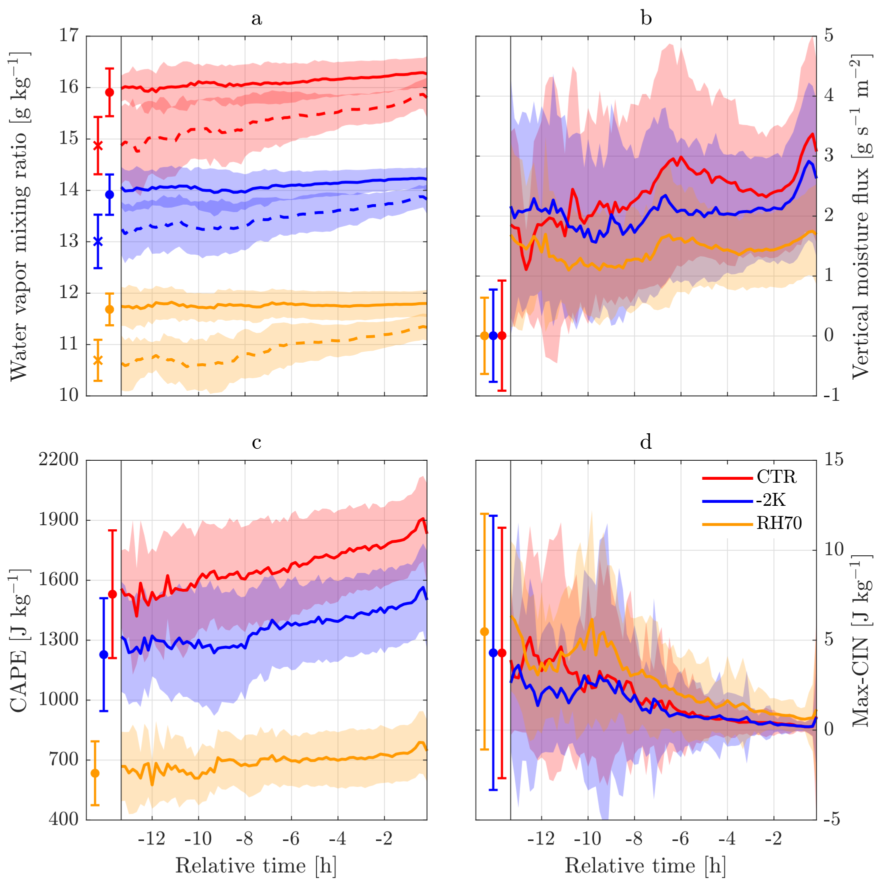

Figure S4. As in Figure 2, but for the full 13.3 h of the aggregate convergence loci.

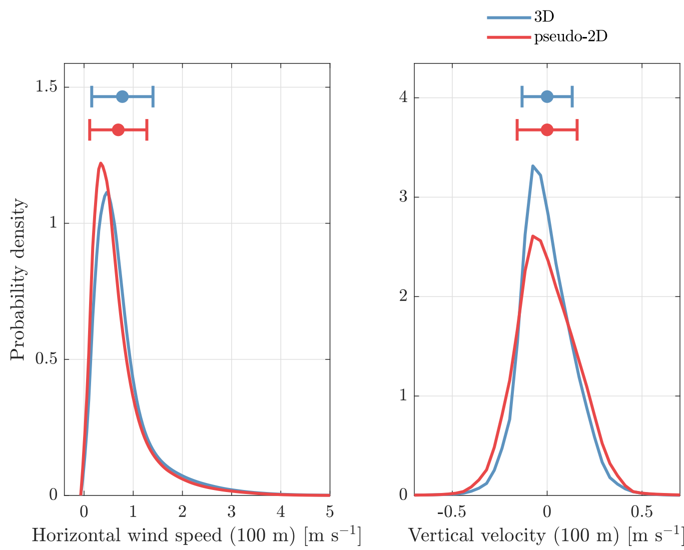

Figure S5. Horizontal and vertical velocities in the pseudo-2D setup (CTR) and in a comparable simulation with horizontal dimensions of equal size (3D). Dots and errorbars show the mean and one standard deviation of the distributions. The 3D simulation is run on the UCLA LES in a 200 km×200 km domain to RCE. The temporal and spatial resolutions (5 min and 400 m, respectively) differ slightly from those used in the 2D setup (10 min and 200 m). The pseudo-2D and 3D simulations are otherwise identical.